



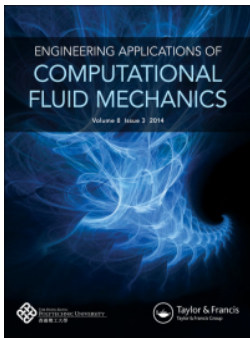
Computational fluid dynamics-multibody system dynamics bidirectional coupling calculation and flow-induced vibration evaluation of a high-speed

Downloaded from: <https://research.chalmers.se>, 2025-07-01 19:44 UTC

Citation for the original published paper (version of record):

Li, Z., Chen, C., Song, H. et al (2025). Computational fluid dynamics-multibody system dynamics bidirectional coupling calculation and flow-induced vibration evaluation of a high-speed pantograph-catenary system. *Engineering Applications of Computational Fluid Mechanics*, 19(1).
<http://dx.doi.org/10.1080/19942060.2025.2512954>

N.B. When citing this work, cite the original published paper.



Computational fluid dynamics-multibody system dynamics bidirectional coupling calculation and flow-induced vibration evaluation of a high-speed pantograph-catenary system

Zhuojun Li, Chunjiang Chen, Huapu Song, Gang Yang, Jun Yang, Huadong Yao & Jiqiang Niu

To cite this article: Zhuojun Li, Chunjiang Chen, Huapu Song, Gang Yang, Jun Yang, Huadong Yao & Jiqiang Niu (2025) Computational fluid dynamics-multibody system dynamics bidirectional coupling calculation and flow-induced vibration evaluation of a high-speed pantograph-catenary system, Engineering Applications of Computational Fluid Mechanics, 19:1, 2512954, DOI: [10.1080/19942060.2025.2512954](https://doi.org/10.1080/19942060.2025.2512954)

To link to this article: <https://doi.org/10.1080/19942060.2025.2512954>



© 2025 The Author(s). Published by Informa UK Limited, trading as Taylor & Francis Group.



Published online: 03 Jun 2025.



Submit your article to this journal [↗](#)



Article views: 67



View related articles [↗](#)



View Crossmark data [↗](#)

Computational fluid dynamics-multibody system dynamics bidirectional coupling calculation and flow-induced vibration evaluation of a high-speed pantograph-catenary system

Zhuojun Li^a, ChunJiang Chen^a, Huapu Song^a, Gang Yang^a, Jun Yang^b, Huadong Yao^{id}^c and Jiqiang Niu^{a,b}

^aSchool of Mechanical Engineering, Southwest Jiaotong University, Chengdu, People's Republic of China; ^bTechnical Research Department, CRRC Industrial Institute (Qingdao) Co., Ltd., Qingdao, People's Republic of China; ^cDepartment of Mechanics and Maritime Sciences, Chalmers University of Technology, Gothenburg, Sweden

ABSTRACT

Increasing the speed of a pantograph deteriorates its aerodynamic performance and aggravates the problem of flow-induced vibration, which is not conducive to the stability of the pantograph – catenary system (PCS). Currently, commercial high-speed trains operate at speeds exceeding 350 km/h, with line test speeds exceeding 450 km/h, making the impact of airflow on pantograph dynamics increasingly significant. Therefore, a simulation study on the bidirectional coupling between pantograph aerodynamics and structural dynamics is urgently needed. This study proposes a bidirectional coupling method for the pantograph based on overset grids. The user-defined functions (UDF) in Fluent enable real-time data exchange between aerodynamic forces and structural displacements. The flow field was modelled using the Shear Stress Transport $k-\omega$ turbulence model and Reynolds-averaged Navier – Stokes equations, and the dynamics is computed by Newmark-Beta solving the differential equations. It was found that the calculation method in this study was reliable and efficient. The motion of the pantograph assembly in the flow field will change the airflow mode, thus affecting the aerodynamic characteristics of the assembly, and the high-frequency and stochastic aerodynamic excitation will lead to an increase in vibration of the pantograph assembly, especially at the contact strip. For example, when the pantograph operated in the knuckle-upstream direction at 450 km/h, it exhibited poor PCS interaction, with a mean contact force of 50 N, a standard deviation of 36 N, and an overall offline rate of 7%. This study introduced a novel approach to pantograph fluid – structure coupling, offering valuable insights for predicting high-speed pantograph performance and evaluating PCS interactions.

ARTICLE HISTORY

Received 16 March 2025
Accepted 22 May 2025

KEYWORDS

High-speed train; pantograph; fluid – structure interaction; flow-induced vibration; pantograph – catenary system (PCS) interaction

1. Introduction

As the current-receiving component on top of a high-speed train, a pantograph plays an important role in obtaining electrical energy, as shown in Figure 1. To ensure that the train obtains stable electric energy during operation, the pantograph contact strip should maintain close contact with the catenary, and the magnitude of the pantograph – catenary system (PCS) contact force should be within a suitable range (Z. Liu et al., 2024). As the speed of the train increases, the flow field around the pantograph deteriorates, and the pantograph generates complex dynamic behaviours under the action of the strong airflow that worsen the quality of the PCS current received. The aerodynamic and PCS dynamics problems involved in pantograph operation at high speeds are highly correlated, and the flow field near the pantograph is affected by its attitude, which in turn depends on the

aerodynamic excitation. Therefore, studying the relationship between the aerodynamic characteristics of a pantograph and the dynamic performance of a PCS during train operation is of great engineering significance.

Many scholars have studied pantographs in high-speed operations based on aerodynamics and structural dynamics. Gregori et al. (2017), Amano et al. (2024), Pappalardo et al. (2015), Massat et al. (2006), Huan et al. (2014), W. Wang et al. (2019), Song et al. (2024), Zhou and Zhang (2011), Seo et al. (2005) studied the dynamic characteristics of a PCS under different working conditions based on the mutual coupling of the pantograph lumped-mass/multi-rigid body model and the finite element model of the catenary; however, none of them involved aerodynamics. Xiao et al. (2020), X. Li et al. (2018), Wu et al. (2020), Gai et al. (2024), Dai et al. (2022a, 2022b), Brambilla et al. (2022), Qin et al.

CONTACT Jiqiang Niu  jiqiang_niu@163.com  School of Mechanical Engineering, Southwest Jiaotong University, Chengdu 610031, Sichuan, People's Republic of China Technical Research Department, CRRC Industrial Institute (Qingdao) Co., Ltd., Qingdao 266000, People's Republic of China

© 2025 The Author(s). Published by Informa UK Limited, trading as Taylor & Francis Group.

This is an Open Access article distributed under the terms of the Creative Commons Attribution-NonCommercial License (<http://creativecommons.org/licenses/by-nc/4.0/>), which permits unrestricted non-commercial use, distribution, and reproduction in any medium, provided the original work is properly cited. The terms on which this article has been published allow the posting of the Accepted Manuscript in a repository by the author(s) or with their consent.

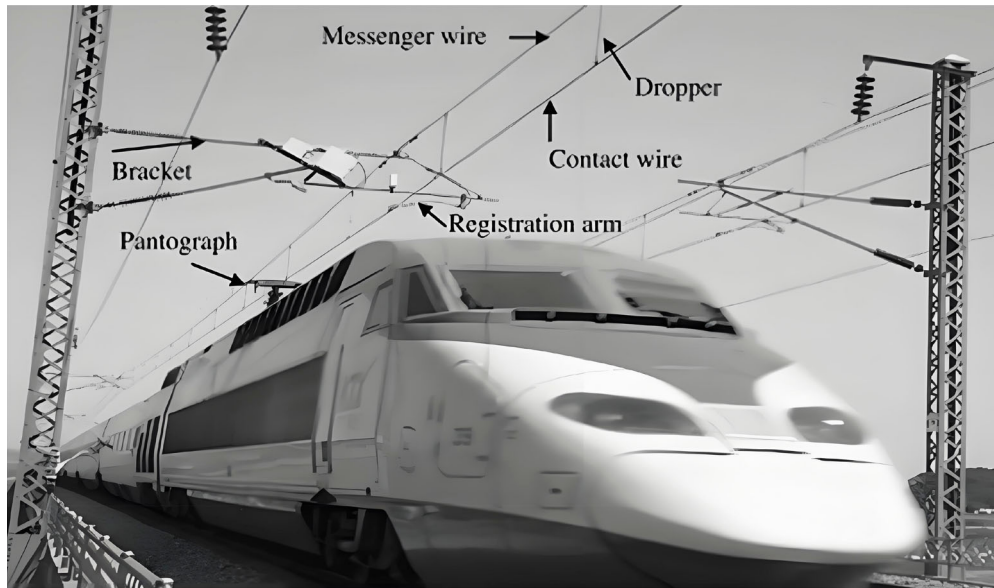


Figure 1. Schematic diagram of the composition of the PCS for high-speed trains.

(2024), Ouyang et al. (2022), H. Liu et al. (2023), H. Liu et al. (2022) carried an aerodynamic simulation of a high-speed pantograph under different working conditions based on different turbulence models but did not consider the dynamic response caused by aerodynamic excitation. Mature research in various fields lays the groundwork for pantograph flow-induced vibration studies. Carnevale et al. (2015) carried out a computational fluid dynamics (CFD) numerical simulation of a pantograph at different speeds based on the Shear Stress Transport (SST) $k-\omega$ model and compared the simulation results with wind tunnel tests, which showed that the faster the pantograph run, the greater the difference between the results obtained by pure fluid simulation and the actual ones, which reflected the influence of the flow-induced vibration on the aerodynamic characteristics of the pantograph when running at high speed.

To make the simulation results more consistent with real conditions, many scholars have considered the coupling relationship between the aerodynamics and dynamics of the pantograph structure. Pantograph lumped-mass and multi-rigid body models are widely used because of their high accuracy and low computational resources. Bocciolone et al. (2006) and R. Li et al. (2016) carried out a CFD numerical simulation of the pantograph based on the $k-\varepsilon$ model, and then investigated the effect of aerodynamic excitation on the PCS dynamics system by using the pantograph lumped-mass model. Dai et al (2022) numerically simulated a high-speed pantograph with baffles based on the SST $k-\omega$ model and applied the computed aerodynamic excitation to the multi-rigid body dynamics model of

the pantograph. They obtained the optimal baffle angle under the optimal PCS contact force by analysing the influence of the baffles on the aerodynamic performance of the pantograph at different angles. The computational results obtained based on the flexible PCS model are more accurate but require huge computational resources. D. Wang et al. (2024) carried out a numerical simulation of a train passing through a tunnel based on the realisable $k-\varepsilon$ model and loaded the obtained aerodynamic excitation on the pantograph flexible model. The results show that the PCS contact force and pantograph displacement increase significantly after the train enters the tunnel. Kulkarni et al. (2016) established a finite element model of a catenary system based on absolute node coordinate formulation (ANCF) beam elements and calculated the aerodynamic excitation using empirical formulas to study the effect of 20 m/s ambient wind on the PCS contact force. Pombo and Ambrósio (2013) established a PCS coupling model based on multi-rigid body dynamics and the finite element method and loaded the aerodynamic forces obtained from a 20 m/s crosswind wind tunnel test into the coupling model, which showed that the average contact force of the PCS increased by 34% under the wind load compared with that in a windless environment.

Compared with unidirectional coupling, bidirectional coupling can more accurately model the relationship between the flow field near the pantograph and its dynamic behaviour. Ji et al. (2021) carried out a high-speed pantograph flow-induced vibration simulation based on a multi-rigid body dynamics model on the joint Fluent – Matlab/Simulink – Simpack platform and compared it with the test data of the Beijing – Shenyang Line train. The average deviation of contact force was

only 0.05%, which verified the correctness of the coupling method.

In conclusion, conducting an accurate study of flow-induced vibration in pantographs through real train tests is challenging due to the long testing time, high costs, and the complexity of external variables. Unidirectional coupling has a certain reliability in the low-speed operation stage of the pantograph. However, as the train speeds up, the vibration of the pantograph intensifies, which makes it difficult to ensure its authenticity. At this stage, research on the coupling effect between the aerodynamics and structural dynamics of high-speed pantographs using bidirectional coupling is relatively limited, and the existing bidirectional coupling methods rely on joint simulation between multiple platforms, which is characterised by low computational efficiency and a long simulation period. In this paper, we proposed a method of tight coupling of the high-speed pantograph flow-induced vibration relying on Fluent as the aerodynamic calculation engine and Fluent user-defined functions (UDF) as the calculation engine of the PCS structural dynamics and the data exchange space, and at the same time, considering the aerodynamic characteristics and dynamic characteristics of the pantograph, an in-depth study of the coupling effect between the two.

2. Modelling instructions

2.1. Geometric model of pantograph

As shown in Figure 2(a–c), the pantograph is located in the sinking platform on the top of the train, and consists of the pan-head at the top, upper arm rod, balance arm, lower arm rod, pull rod, fairing in the middle, and insulators at the bottom, with outer contour dimensions of $2.34\text{ m} \times 1.94\text{ m} \times 1.58\text{ m}$. As shown in Figure 2(d), the pantograph frame is a four-link mechanism with a spring-damped connection between the pan-head and contact strip.

2.2. Computational domain

From the perspective of improving the computational timeliness and focusing on the aerodynamic performance of the pantograph and the evolution of the surrounding flow field, the upper half of the vehicle body was cut off for the construction of the computational domain, as shown in Figure 3, and the dimension of the computational domain was $15.5\text{ m} \times 6\text{ m} \times 4\text{ m}$. The pantograph was located 4 m downstream of the inlet boundary of the computational domain, and the outlet boundary of the computational domain was situated 10 m away from the pantograph. From the computational domain, the ratio of

the windward surface of the pantograph (the projected area in the incoming flow direction is 0.592 m^2) to the cross-section of the computational domain was approximately 2.5%, meeting the requirement of the EN 14067 standard (2018) (the blockage ratio is less than 5%). To simulate the aerodynamic performance of the pantograph, the boundary conditions were defined as follows: the upstream boundary of the computational domain was defined as a velocity inlet, and the velocity was the speed of the vehicle (Dai et al., 2022); the downstream boundary of the computational domain was defined as a pressure outlet, and the static pressure was 0 Pa; the top, bottom, left, and right four surfaces of the computational domain were defined as slip fixed walls, and the slip speed was the speed of the vehicle.

2.3. Grid generation

An overset grid was used to process the computational domain grid, and six overset regions were set around the contact strip, panhead, upper frame, lower arm rod, pull rod, and fairing insulators. Refined grid processing was used around the pantograph. Two sets of refine boxes (1 and 2) were set up, whose locations are shown in Figure 4(a), and the dimensions of regions 1 and 2 were $8.2\text{ m} \times 4\text{ m} \times 2.5$ and $3.8\text{ m} \times 2.4\text{ m} \times 2\text{ m}$, respectively. As shown in Figure 4(b–d), for the pantograph and the fairing, six layers of grid were set up in the boundary layer regions of the near-wall surfaces, with the thickness of the first layer being 0.3 mm to capture the fine flows on their near-wall surfaces.

2.4. Solution method and settings

Based on the incompressible (H. Liu et al., 2022; Kim et al., 2023; Zhao et al., 2020) transient mean Reynolds number N - S equation and the SST k - ω turbulence model, the time term in the discrete double-step method with second-order accuracy in the centre-difference format was used with a time step length of $1.0 \times 10^{-3}\text{ s}$, 10 iterations within the step, and the residuals of the equations in each step were lower than 10^{-3} . A total of 2000 time steps were calculated, of which the first 400 steps were used to obtain a stable and fully developed pantograph flow field, and the second 1600 steps (defining the airflow through the sinking platform as one cycle, namely 200 steps, for a total of 8 cycles) were used to construct the pantograph flow field.

2.5. Grid independence analysis

To reduce costs and improve efficiency, and considering the pantograph's basic symmetry, a model of the upper

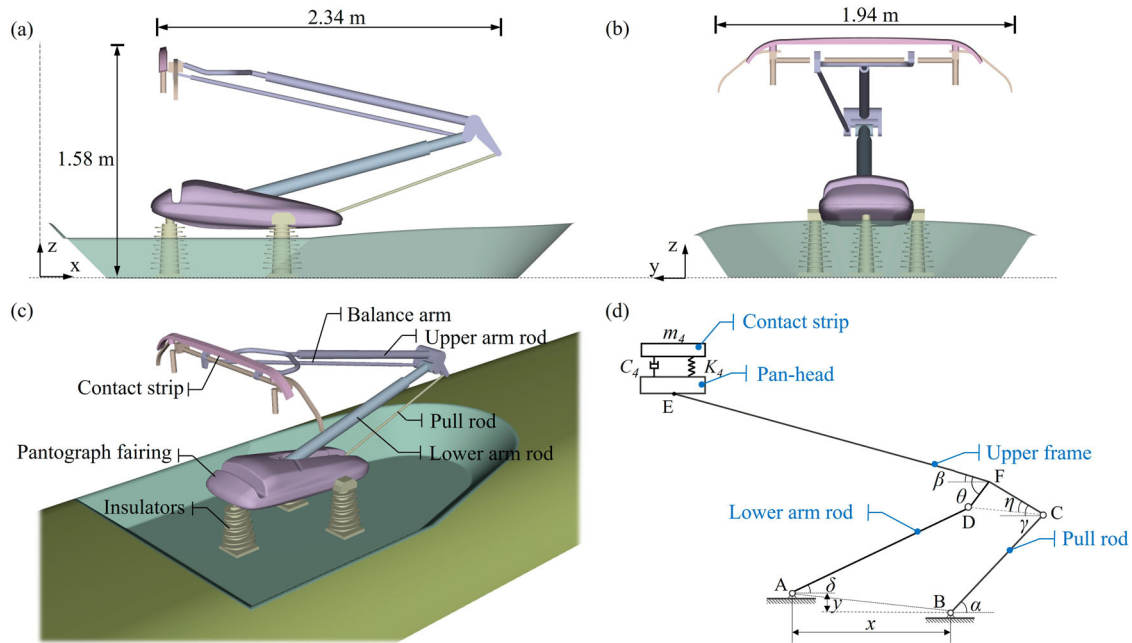


Figure 2. (a) Side view, (b) front view, (c) 3D view of the pantograph model, and (d) a sketch of the mechanism.

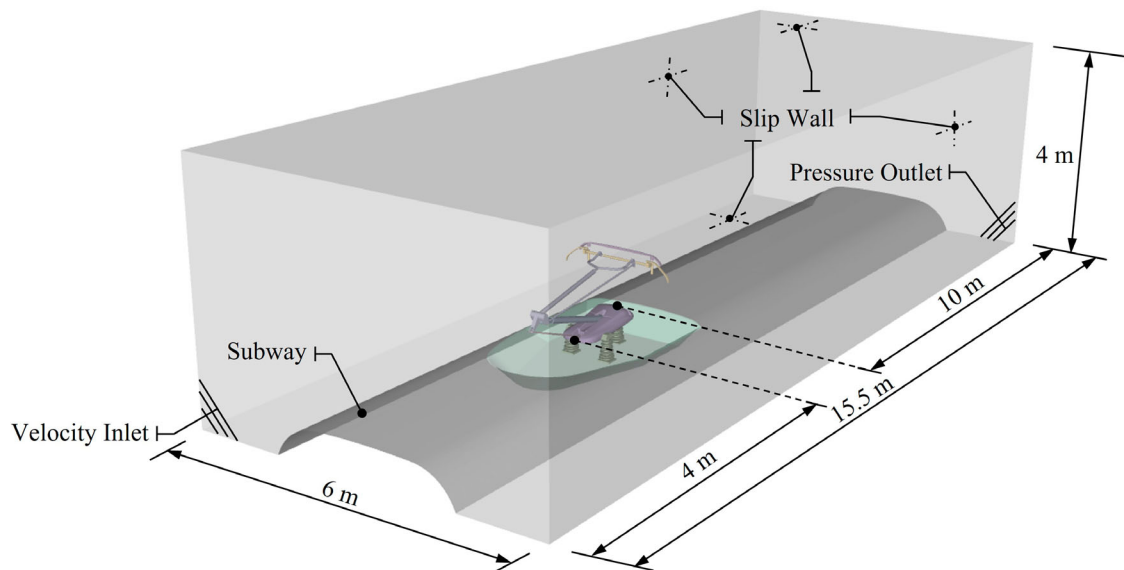


Figure 3. Definition of the main dimensions and boundaries of the computational domain of a full-size pantograph.

pantograph (including the pan-head and part of the upper framework) was selected for grid independence verification, as shown in Figure 5(a). The dimensions of the computational domain were $8\text{ m} \times 6\text{ m} \times 3\text{ m}$, with boundary conditions matching those outlined in Section 2.2 of this study. Two grid sets (Cell-1 and Cell-2) were generated using different surface grid sizes (2 and 1 mm), based on the overset grid technique, resulting in cell numbers of 10.45 and 21.16 million, respectively, as shown in Figure 4(b). As depicted in Figure 5(c), the deviations in both drag force and lift between Cell-1

and Cell-2 were less than 2%. Overall, the CFD results for Cell-1 and Cell-2 were very similar, indicating that the grid resolution used in this section is sufficient for simulating the pantograph aerodynamic performance. However, to improve computational efficiency, the grid resolution of Cell-1 was chosen for the subsequent calculations.

As shown in Figure 6, there was no significant difference in the three-dimensional streamline distribution around the pantograph when computed using Cell-1 and Cell-2. The high-speed airflow was obstructed by the

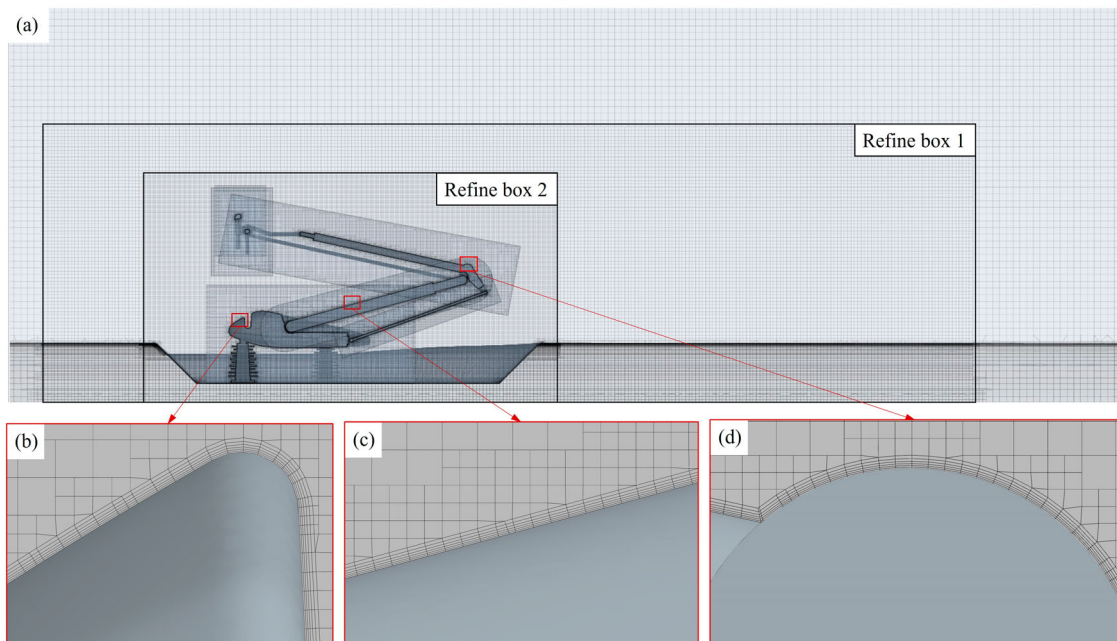


Figure 4. Pantograph (a) refine box setup, and boundary layer grids for the (b) fairing, (c) lower arm rod, and (d) upper arm rod.

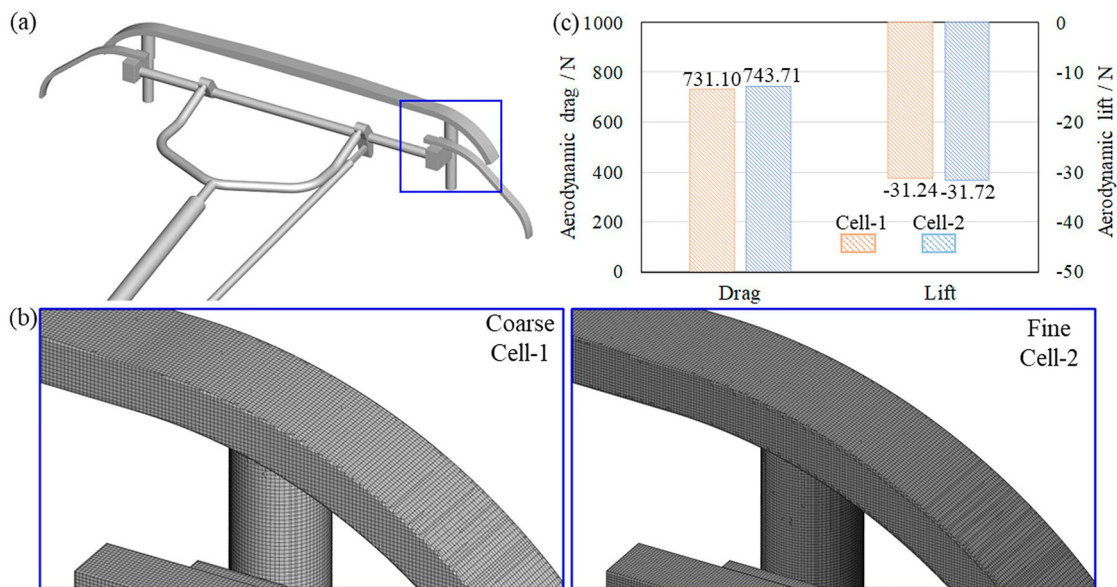


Figure 5. (a) The model used for grid independence analysis, along with the (b) coarse and fine grids, as well as (c) the results of the calculations under train speed of 350 km/h.

carbon contact strip and the pan head support, creating a separated vortices. As indicated by the arrows in the figure, part of the airflow follows the rear surface of the carbon contact strip towards its ends, disturbing the airflow passing through the circular strut at the bottom of the carbon contact strip. Two pairs of separating vortices (Vortices 1 and Vortices 2) can be observed downstream of the carbon contact strip and pan-head support in the $Y = 0$ plane. The scale of the separated vortices ($x_i = y_i$, $i = 1, 2, 3$), computed using both Cell-1 and Cell-2, were essentially identical.

3. Dynamics model of PCS

3.1. MSD model of pantograph

3.1.1. Lumped-mass model

The lumped-mass and multi-rigid body models were commonly used in the dynamic analysis of pantographs. The natural frequency of pantographs typically falls within the low-frequency range, and to reduce the computational effort of bidirectionally coupled flow-induced vibration calculations, a lumped-mass model was used to study their natural frequency. And its effectiveness had

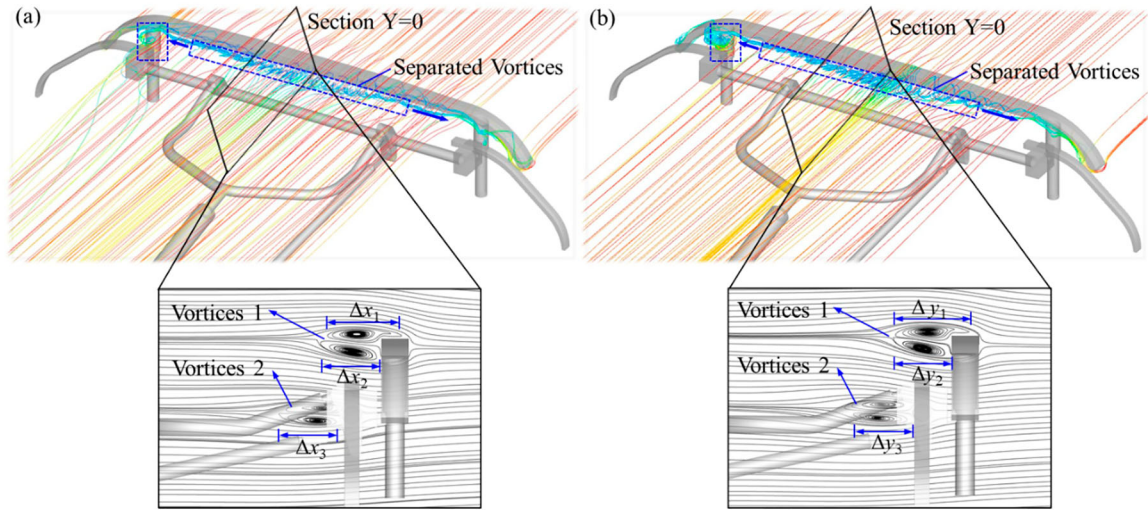


Figure 6. The three-dimensional streamline distributions of the pantographs, along with the velocity contour and streamlines on the plane of symmetry, using (a) Cell-1 and (b) Cell-2 as the computational grids, respectively.

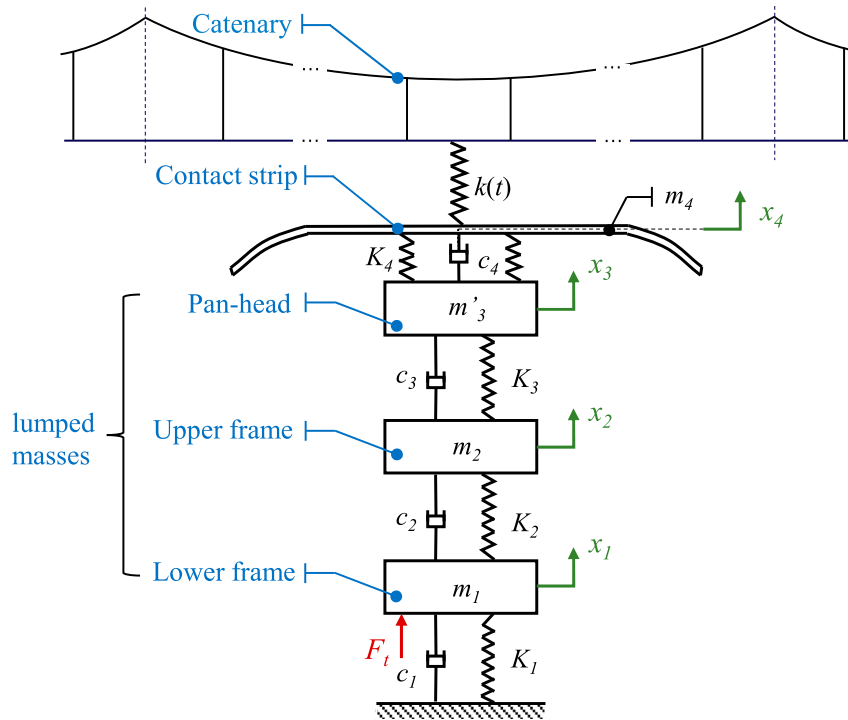


Figure 7. Lumped-mass model of pantograph.

been proven in PCS simulations (Song et al., 2020, 2024; Tur et al., 2015). As shown in Figure 7, the lumped masses m_1 , m_2 , and m'_3 of the pantograph rods interact with each other in the vertical direction through spring damping. The spring sleeve between the contact strip m_4 and the pan-head was directly simulated by K_4 and c_4 , and $k(t)$ was the contact stiffness of the PCS.

The Newmark-Beta method is widely used for solving the dynamical equations of pantographs because of its excellent accuracy and stability (Ambrósio et al., 2012; Rong et al., 2019; Song et al., 2020), so this method

was used to solve the following differential equations of motion for the pantograph lumped-mass:

$$\mathbf{M} \frac{d^2[\mathbf{q}(t)]}{dt^2} + \mathbf{K}\mathbf{q}(t) + \mathbf{C} \frac{d[\mathbf{q}(t)]}{dt} = \mathbf{F}(t) \quad (1)$$

$$\mathbf{q}(t) = \{x_1(t) \ x_2(t) \ x_3(t) \ x_4(t)\}^T \quad (2)$$

$$\mathbf{F}(t) = \{F_{L1}(t) + F_t \quad F_{L2}(t) \quad F_{L3}(t) \quad F_{L4}(t) - F_c\}^T \quad (3)$$

Table 1. Dynamic and geometric parameters of the components of the pantograph model.

Mass	Value/kg	Spring	Value/(N·m ⁻¹)	Damping	Value/(N·s·m ⁻¹)
m_1	11.413	K_1	130	c_1	300
m_2	5.475	K_2	60000	c_2	0
m'_3	3.728	K_3	8400	c_3	48
m_4	1.550	K_4	8200	c_4	200

where $\mathbf{q}(t)$ and $\mathbf{F}(t)$ are system displacement and load vectors; $F_{Li}(t)$ ($i = 1, 2, 3, 4$) is the aerodynamic lifting force on the lower arm rod, upper frame, pan-head, and contact strip, which is computed using Fluent; F_t is the static lifting force provided by the pantograph airbag, which acts on the lower arm rod; F_c is the contact force of the PCS; and \mathbf{M} , \mathbf{K} , and \mathbf{C} are the system mass, stiffness, and damping matrices, respectively.

The relevant parameters of the pantograph dynamics model were shown in Table 1.

3.1.2. Kinematic constraint relationship

Based on the sketch of the pantograph mechanism in Figure 2(d), the kinematic constraint Equations (4)–(6) for the pantograph are listed.

The pan-head is constrained to the base of the lower arm rod as follows:

$$\Phi_1 = \overline{EF} \cdot \sin \beta + \overline{DF} \cdot \sin(\theta - \beta) + \overline{AD} \cdot \sin \delta + y_A - Y_E = 0 \quad (4)$$

$$\Phi_2 = \overline{EF} \cdot \cos \beta - \overline{DF} \cdot \cos(\theta - \beta) - \overline{AD} \cdot \cos \delta + x_A - X_E = 0 \quad (5)$$

where x_A, y_A, Y_E, X_E are the coordinates of the articulation point A of the lower arm rod and the coordinates of the articulation point E of the pan-head and the upper frame; and δ, β are the angles between the lower arm rod, the upper frame \overline{EF} and the horizontal direction. θ is the angle between the rod DF and EF.

The constraint relationship between the lower arm rod and pull rod is as follows:

$$\Phi_3 = x^2 + y^2 + \overline{AD}^2 - 2\overline{AD} \cdot \sqrt{x^2 + y^2} \cdot \cos\left(\beta + \tan^{-1}\frac{y}{x}\right) - CD^2 - \overline{BC}^2 + 2\overline{BC} \cdot CD \cdot \cos(\alpha + \gamma - \eta) = 0 \quad (6)$$

where x, y for the lower arm rod articulation point A and the pull rod articulation point B in the longitudinal and vertical distance; α and γ are the angles between the pull rod, the upper frame \overline{CF} , and the horizontal direction. η is the angle between the rod CF and the line CD.

3.2. Contact between pantograph and catenary

Current simulations of pantograph flow-induced vibrations mainly focus on the pantograph itself, with the catenary typically introduced as an external excitation. Due to the significant difference in characteristic length scales between the pantograph and the catenary, it remains challenging to conduct cross-scale flow field simulations. In the initial state, the contact wire generated a certain sag in the vertical direction under the action of gravity, which had a greater influence on the subsequent calculation of the contact state of the PCS (Zhou & Zhang, 2011). Therefore, it is necessary to first calculate the initial equilibrium state of the contact wire, and then perform a dynamic simulation of the PCS contact. The dropper point on the contact wire was set as the coordinate origin, and the static shape of its arbitrary position was obtained using Equation (7).

$$y_c = \begin{cases} \frac{\rho_{CW} g x(x - x_{d1})}{2T_{CW}} & (x < x_{d1}) \\ \frac{\rho_{CW} g(x - x_{di})(x - x_{di+1})}{2T_{CW}} & (x_{di} < x < x_{di+1}) \\ \frac{\rho_{CW} g(x - x_{dn})(x - L_s)}{2T_{CW}} & (i = 1, 2, 3, \dots, n - 1) \\ & (x < L_s) \end{cases} \quad (7)$$

where x, L_s, x_{di} ($i = 1, 2, 3, \dots, n$), and ρ_{CW} are the longitudinal coordinates of the contact wire, the span of the catenary, the location of the droppers, and the density of the contact wire, respectively; T_{CW} is the tension of the contact wire, and g is the acceleration of gravity.

In order to simplify the catenary model and to make it meet the requirements of engineering calculations. The catenary stiffness was calculated using the finite element method, and the results were fitted to obtain the catenary stiffness and time t relationship (Guo et al., 2005), as shown in Equation (8).

$$k(t) = k_0 \left[1 + k_1 \cos \frac{2\pi vt}{L} + k_2 \cos \frac{2\pi vt}{L_1} + k_3 \cos^2 \frac{2\pi vt}{L} + k_4 \cos^2 \frac{\pi vt}{L} + k_5 \cos^2 \frac{2\pi vt}{L_1} \right] \quad (8)$$

where k_0 denotes the average stiffness coefficient, k_1, k_2, \dots, k_5 denote the stiffness variation coefficients, L_1 is the distance between neighbouring droppers, and v denotes the vehicle speed. And $k_0 = 82,300$ N/m, $L_1 = 8$ m, $k_1 = 0.467$ N/m, $k_2 = 0.083$ N/m, $k_3 = 0.260$ N/m, $k_4 = -0.280$ N/m, $k_5 = -0.336$ N/m, and $L = 50$ m.

The contact between the catenary and contact strip of the pantograph was modelled using the penalty function method (Mei et al., 2022; Song et al., 2017, 2024). The PCS contact was divided into two states: contact ($y_h \geq y_c$) and offline ($y_h < y_c$). The contact force F_c can

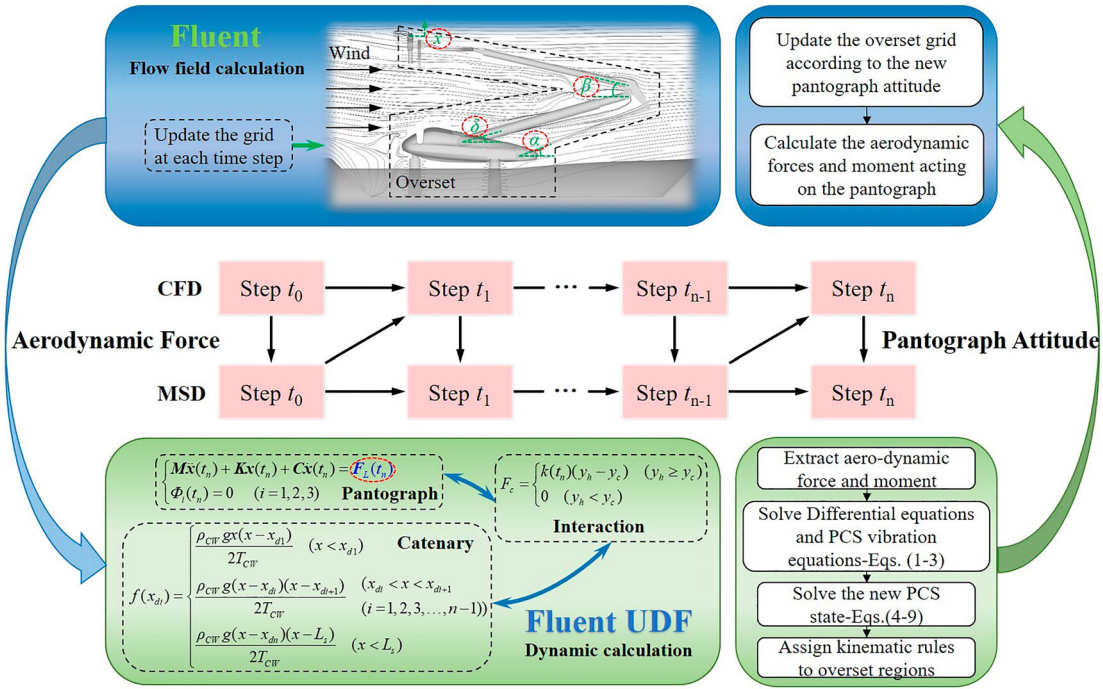


Figure 8. Calculation flow of flow-structure bidirectional coupling of PCS.

be calculated using Equation (9) when the pantograph and catenary are in contact.

$$F_c = \begin{cases} k(t)(y_h - y_c) & (y_h \geq y_c) \\ 0 & (y_h < y_c) \end{cases} \quad (9)$$

where y_h and y_c are the contact strip and wire displacements, respectively.

4. Solution methods and verification

4.1. Bidirectional coupling methods

As shown in Figure 8, under the same time step, Fluent and C programming were used to realise the pantograph aerodynamic performance simulation and dynamics calculation, respectively, and the real-time interaction of the aerodynamic and dynamic data was realised through the UDF function. The basic process is as follows: obtain the aerodynamic forces of each component of the pantograph in the current attitude based on Fluent, extract the aerodynamic forces of each component through the UDF function, use the dynamic code to obtain the dynamic parameters of the pantograph under the current aerodynamic load, calculate the attitude of each component of the pantograph based on the motion of the pantograph mechanism and the pantograph-catenary relationship, and finally update the grids around the pantograph using the overset grid technique to complete the cycle in one time step.

4.2. Verification

4.2.1. Flow around a square cylinder

The Reynolds number of the wind tunnel test is approximately 3.1×10^5 , which is close to the Reynolds number of the pantograph aerodynamic simulation in this paper, and the cross-sectional size of the wind tunnel test section is $0.3 \text{ m} \times 0.4 \text{ m}$. The test speed was 0.56 Ma . The cross section of the square column used for this test was $25 \text{ mm} \times 25 \text{ mm}$, and its length was 300 mm . Based on the parameters of the wind tunnel working condition and the test conditions, the computational domain of the simulation was established, the grid was generated, and the boundaries were defined, as shown in Figure 9(a,b).

Based on the SST $k-\omega$ turbulence model, a double-step control time advancement in second-order accuracy central difference scheme was used, with a physical step length of $1.5 \times 10^{-5} \text{ s}$, 20 iterations within a step, and residuals of each equation lower than 10^{-3} ; a total of 8000 time steps were computed, with the first 4000 steps being used to obtain the stable and fully developed flow field of the square column, and the last 4000 steps being used for time-averaged data sampling. The windward surface of the square column ($25 \text{ mm} \times 300 \text{ mm}$) and a wind speed of 185 m/s (0.56 Ma) were selected as the reference values, and the results of the aerodynamic drag and pressure calculations of the square column were dimensionless. As shown in Figure 9(c), the calculated values of the surface pressure coefficient of the square column distributed along its circumferential direction are consistent with the

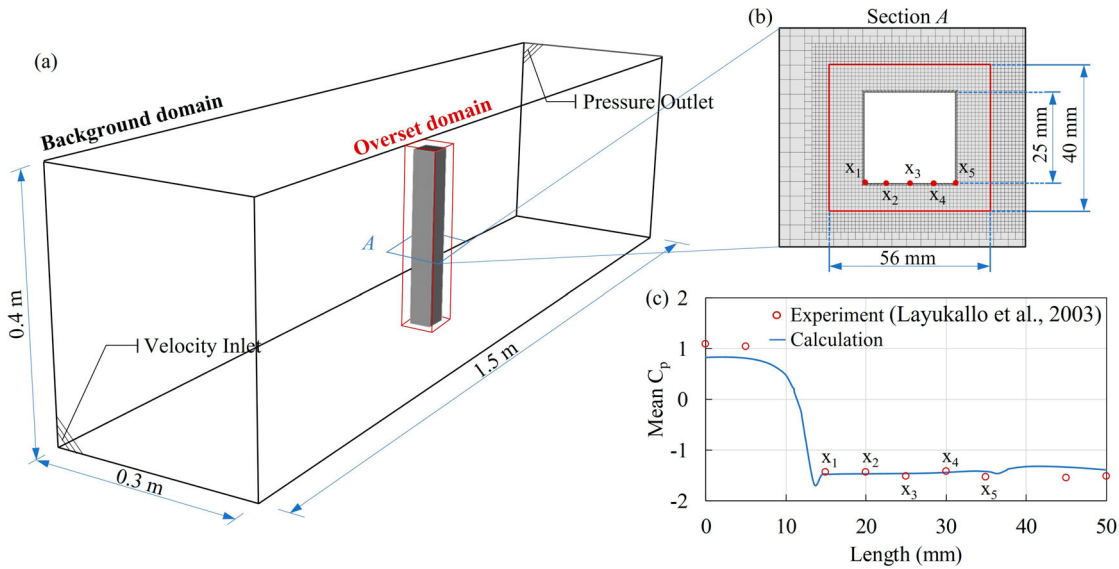


Figure 9. (a) Computational domain, (b) cross-sectional dimensions of the square column model (wind speed $0.56 Ma$) used for verification; and (c) comparison of the experimental and computational results for the distribution of surface pressure coefficients along the circumference of a square column.

experimental values (Layukallo & Nakamura, 2003), and the difference between the two was larger at individual positions, with an overall difference below 10.5%. For the aerodynamic drag coefficient of the square column, the difference between the calculated (2.35) and test (2.26) results was less than 4.0%. This indicates that the adopted calculation method and parameter settings satisfied the requirements for simulating the pantograph flow field.

4.2.2. Vortex-induced vibrations of a circular cylinder

Based on a cylindrical flow-induced vibration test in the literature (Chang, 2010), a Reynolds number of 9.7×10^4 and an incoming flow velocity of 1.242 m/s were selected for the verification, in which the diameter of the cylinder D was 0.0889 m, its mass m_{osc} was 9.78 kg, the stiffness and damping of the oscillating system were 775 N/m and 3 Ns/m, respectively, and the natural frequency in water $f_{n,water}$ was 1.12 Hz. A two-dimensional equivalent model was used in the calculation; the dynamic model is shown in Figure 10(a).

As shown in Figure 10(b), the computational domain consists of a background grid ($50D \times 50D$) and an overset grid ($6.7D \times 6.7D$). The cylinder was at a distance of $25D$ downstream from the inlet boundary of the computational domain, where the inlet and outlet boundaries of the computational domain were defined as velocity inlet and pressure outlet, respectively (the static pressure is 0 Pa), and the boundaries of both sides of the cylinder were set as fixed walls. The grid around the cylinder was refined to accurately minimise the flow. To simulate the flow field in the near-wall region of the cylinder

more accurately, six layers of the boundary grid were set up with a growth factor of 1.01, and the first layer was 2×10^{-5} m to satisfy $y^+ < 1$.

The pressure-based solver was selected to carry out the cylindrical flow-induced vibration simulation using the unsteady Navier–Stokes (N–S) equation and the SST $k-\omega$ two-equation turbulence model, and the overset grid was updated after each time step, with a computational time step 0.01 s, and a total computation time of 20 s. In the calculation results, the amplitude ratio and frequency ratio (0.604, 1.340) of the flow-induced vibration of the square column differ from the experimental amplitude and frequency ratio (0.650, 1.256) by 7.1% and 6.7%, respectively, and the average error was less than 7%, which proves the feasibility of the method for calculating the flow-induced vibration in this study.

4.2.3. Comparison with data in literature and EN standard

4.2.3.1. Comparison of PCS coupling model based on literature data. Based on the PCS coupling dynamics model in Chapter 3, and using $0.00097v^2 + 70$ as the average contact force formula, the PCS dynamics simulation was carried out under different pan-head masses at a speed of 300 km/h, and the simulation results were compared with those in the literature (Pombo & Ambrósio, 2012). The dynamics parameters of the PCS coupling model were as follows: catenary span $L_s = 54$ m, contact wire density $\rho_{cw} = 1.33 \text{ kg m}^{-1}$, contact wire tension $T_{cw} = 20$ kN, and spacing between neighbouring droppers $L_1 = 6.75$ m. The lumped-mass of each pantograph

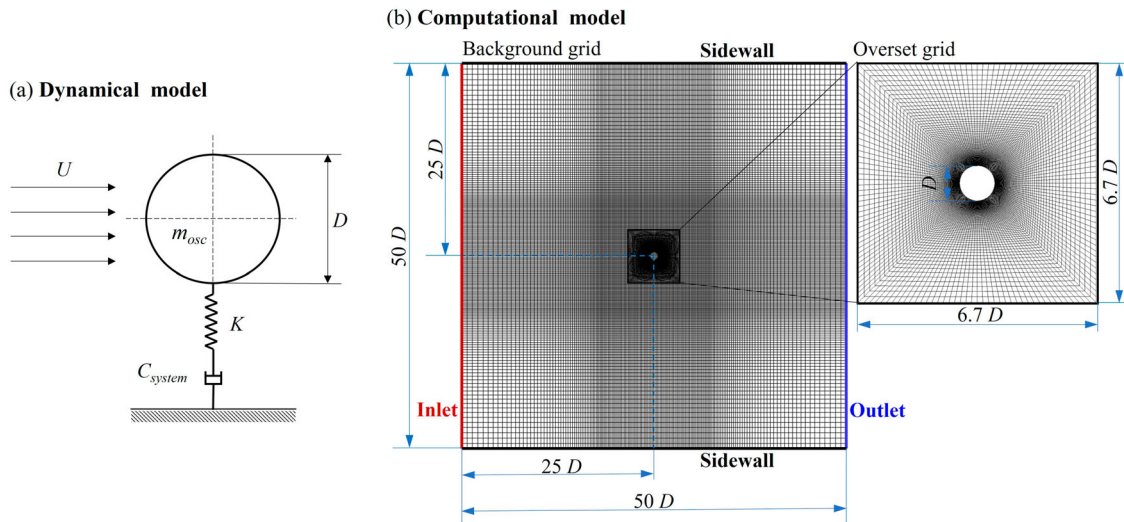


Figure 10. Computational modelling of flow around a circular cylinder. (a) dynamical model, (b) CFD computational domain.

Table 2. Comparison of simulation results with literature for various evaluation indexes of contact force at 300 km/h with different pan-head mass.

Item	Pan-head mass (kg)								Deviation
	6.5		7.5		8.5		9.5		
	Sim.	Lit.	Sim.	Lit.	Sim.	Lit.	Sim.	Lit.	
Maximum (F_{\max})	280.15	267.59	277.08	285.46	274.50	301.84	273.20	300.85	6.47%
Minimum (F_{\min})	74.17	78.94	75.56	74.47	75.19	64.04	74.63	67.52	8.86%
Amplitude ($F_{\max} - F_{\min}$)	205.97	189.15	201.52	210.99	199.31	238.30	198.57	233.83	11.21%
Mean (F_{avg})	162.20	157.38	162.20	157.87	162.19	157.38	162.17	157.38	2.98%
Standard Deviation (σ)	50.09	38.72	48.92	42.20	48.53	44.68	47.56	47.66	13.53%
Deviation	10.41%		5.51%		10.90%		7.61%		8.61%

component m_1 and m_2 were 4.80 and 4.63 kg, respectively, the equivalent stiffnesses K_1 , K_2 , and K_3 were 1, 5400, and 6045 N/m, respectively, and the equivalent damping values C_1 , C_2 , and C_3 were 32, 5, and 10 Ns m^{-1} , respectively. As presented in Table 2, in terms of the contact force evaluation indices, the standard deviation of the simulation results exhibited the largest difference from the literature (13.53%), whereas the mean value exhibited the smallest difference (2.98%). In terms of pan-head mass, the largest difference (10.90%) was found when the pan-head mass was 8.5 kg and the smallest difference (5.51%) was found when the mass was 7.5 kg. Overall, the overall deviation of the simulation from the literature was 8.61%, and the PCS coupling model used in this study was reliable.

4.2.3.2. Comparison of flow-induced vibration data based on EN standard. Based on EN50367 (2020), EN50317 (2012), and EN50119 (2020), the reliability evaluation standard of the pantograph fluid – structure coupling calculation was determined. The EN standard stipulates that $0.00097v^2 + 70$ be used as the formula for the average contact force, where v is the train travelling speed, which was used as the initial value to verify the

feasibility of the pantograph model. The evaluation criteria of the PCS coupling model involved in this study were as follows: the standard deviation of the contact force is less than 0.3 times \times the average contact force, the maximum contact force is less than 350 N, and the vertical maximum amplitude of the pantograph is less than 80 mm. The correctness of the model used in this study was verified based on the above criteria.

Based on the CFD modelling method described in Section 2, an aerodynamic model of the pantograph without fairing in the knuckle-upstream direction was established at a speed of 250 km/h. Based on the 4.1 fluid – structure coupling calculation method, the dynamics and geometric parameters in Table 1 were used to perform the dynamic simulation of the PCS. In Figure 11(a), the black box represents an enlarged diagram of the aerodynamic lifting force from 1.5–3.5 s. The pantograph lifting force is in a downward pressure state and fluctuates significantly, which is not conducive to stable contact of the PCS. From Figure 11(b), it can be observed that the random, strongly pulsating high-frequency excitation of the pantograph aerodynamic lifting force exacerbates the vibration of the PCS, and the standard deviation of the contact force obtained from the fluid – structure coupling

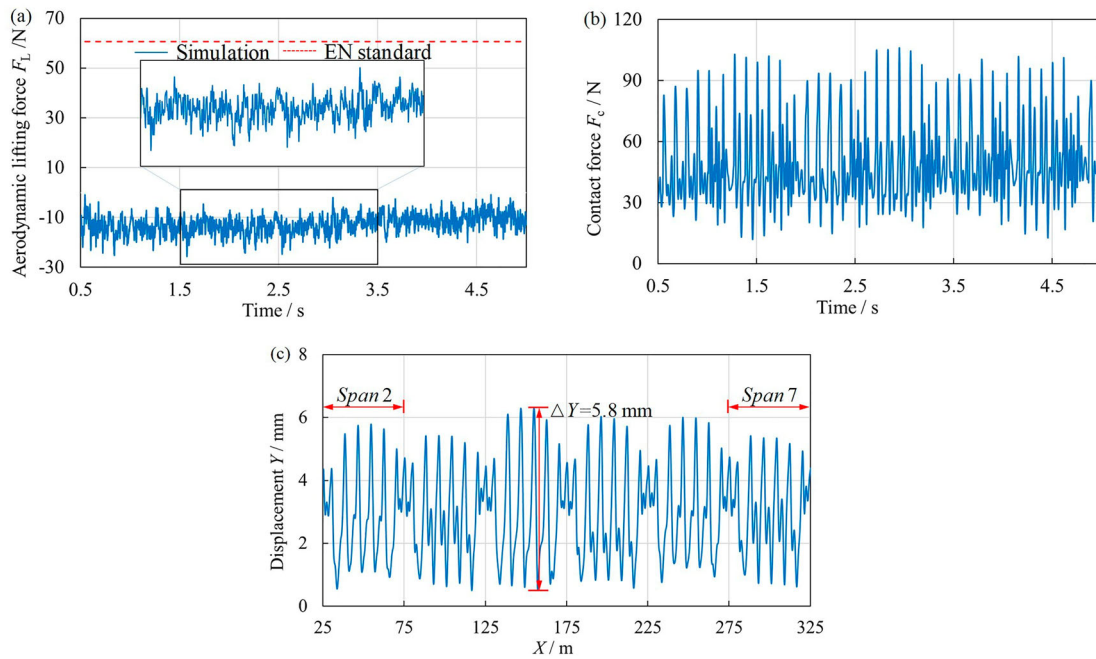


Figure 11. Time-history curves of (a) Aerodynamic lifting force of pantograph, (b) PCS contact force and (c) vertical displacement of PCS contact point under the speed of 250 km/h, with pantograph in the knuckle-upstream direction and without fairing.

calculation (18.51 N) exceeds (by approximately 28%) the requirement of the EN standard (14.484 N). This was due to the fact that this study was based on the real pantograph model and obtained the true aerodynamic force by Fluent computation, which had significant differences with the EN standard because the calculation formula was different.

As shown in Figure 11(c), the calculation results of spans 2–7 were taken and analysed, and the maximum amplitude in the vertical direction of the PCS contact point was 5.8 mm with the centre of mass of the contact strip as the reference point. The calculation results show that the maximum amplitude of the pantograph was within the permissible value of 80 mm specified in the EN standard.

5. Results and discussion

5.1. Aerodynamic characteristics

5.1.1. Aerodynamic force

When the train was running at high speed, the aerodynamic lifting force of the pantograph had a significant influence on the PCS contact state and the PCS flow stability. The mean value and standard deviation were used to analyse the influence of the CFD calculation and bidirectional coupling calculation method on the aerodynamic lifting force of the pantograph in the knuckle-upstream direction at a speed of 450 km/h. As shown in Figure 12(a), the two calculation methods yielded a

significant difference in the aerodynamic lifting force of the pantograph; from the mean value of the aerodynamic lifting force, the lifting force of the pantograph obtained by the CFD calculation is in a slightly lifted state, whereas the lifting force of the pantograph obtained by the bidirectional coupling calculation was in a downward pressure state, with the former being 0.01 N and the latter being -18.67 N. From the view of the standard deviation of the lifting force, the former was 20.57 N, and the latter was 12.18 N.

At the end of the pantograph mechanism, the pan-head contact strip was in direct contact with the contact wire, and its aerodynamic performance affects the PCS. As shown in Figure 12(b), the lifting force of the contact strip obtained by the two calculation methods were both in the state of downward pressure, which was 181.15 N in the CFD method and 209.85 N in the latter method; in terms of standard deviation, it is 10.60 N in the former method and 6.10 N in the latter method. The motion of the pantograph component had a significant influence on the aerodynamic lift force of the pantograph and contact strip, which increases the downward pressure of the pantograph and reduces force fluctuation.

5.1.2. Flow field

The pantograph flow field was analysed in order to study the variation of the flow field under the coupling effect. As shown in Figure 13, the airflow was blocked at the contact strip, and a low-velocity region was formed downstream of it owing to the separation and reflux of the airflow

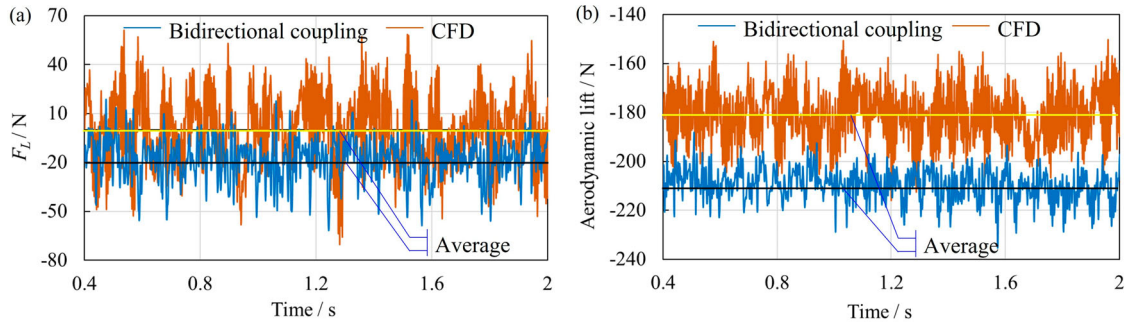


Figure 12. Time-history curves of (a) pantograph aerodynamic lifting force and (b) contact strip lifting force time course curves obtained based on CFD/bidirectional coupling method at 450 km/h, knuckle-upstream condition.

at the upper and lower sides of the contact strip and the formation of a separated vortex. As shown in the black box in the figure, the separated vortex structures obtained by the CFD method and the bidirectional coupling method were quite different; the former forms a pair of internal vortices at the downstream of the contact strip, whereas the latter formed only one separated vortex, but the separation vortex scale of the latter was larger than that of the former ($\Delta X_1 < \Delta X_2$). This is because, under the action of airflow, the coupled condition pantograph frame was lifted up as a whole, but the contact strip cannot be lifted with the frame under the action of aerodynamic downforce and the contact force of the PCS. Further, the spacing between the contact strip and the pan-head support becomes narrower ($\Delta Z_1 > \Delta Z_2$), the airflow through the bottom surface of the contact strip was reduced, and the blocking effect by the pan-head support was strengthened, which results in the change of the structure of the separated vortex. As indicated by the red arrows in the blue box in the figure, under the influence of the vortex structure, the turbulence of the contact strip backwash was larger in the CFD method than in the coupling method, and the airflow was oscillating and more turbulent. This was one of the possible reasons for the larger standard deviation of the lift force of the contact strip in the CFD method calculation results.

As shown in Figure 14, for the pantograph in knuckle-upstream direction, vortex shedding primarily occurs downstream of the fairing, at the articulation between the lower arm rod and the upper frame, and around the pan-head and carbon contact strip. In region 1 of the figure, compared with the coupled condition, the vortex downstream of the carbon contact strip in the uncoupled condition was more turbulent, and the amount of vortex shedding was larger. This observation was consistent with the streamline distribution pattern shown in Figure 13 and was one of the main reasons why the lift amplitude of the carbon contact strip in the uncoupled condition was significantly larger than in the coupled condition. In

region 2 of the figure, compared with the uncoupled condition, the amount of vortex shedding in the upper frame curved rod and middle section of the pan-head increased significantly under the coupled condition. This occurred because, under the uncoupled condition, the tail flow formed at the upper frame curved rod was blocked by the middle section of the pan-head and cannot fully develop. In contrast, under the coupled condition, the upper frame lifted up, causing a vertical displacement between the upper frame curved rod and the pan-head. As a result, the vortex at the tail of the upper frame curved rod had more space to develop, leading to an increase in vortex shedding. The changes in vortex shedding in region 3 were also related to the motion of the pantograph components.

5.2. Transient dynamic response

Under aerodynamic excitation, the pantograph exhibited a complex structural response. As shown in Figure 15(a,b), the amplitude of the lower arm rod tilt angle was small during train operation, and the main frequency of the vibration response of the lower arm rod was concentrated in the interval of 0–5 Hz, the amplitude of the response is small, which was a low-frequency response, with a fundamental frequency of 1.248 Hz connected to its multiple frequencies through the folding line. The red and orange lines in the figure represent the theoretical values of the frequency of the pantograph passing through the registration arm and the dropper, respectively. The figure showed that the fundamental frequency of the vibration of the lower arm rod and its multiple frequencies was mainly distributed near the red line, which indicates that the main factor affecting the dynamic response of the lower arm rod was the dynamic behaviour of the pantograph at the registration arm. As can be observed from Figure 15(c), the position change of the contact point had an obvious periodical pattern compared to the lower arm rod tilt angle, and the period was the time required to pass through one span

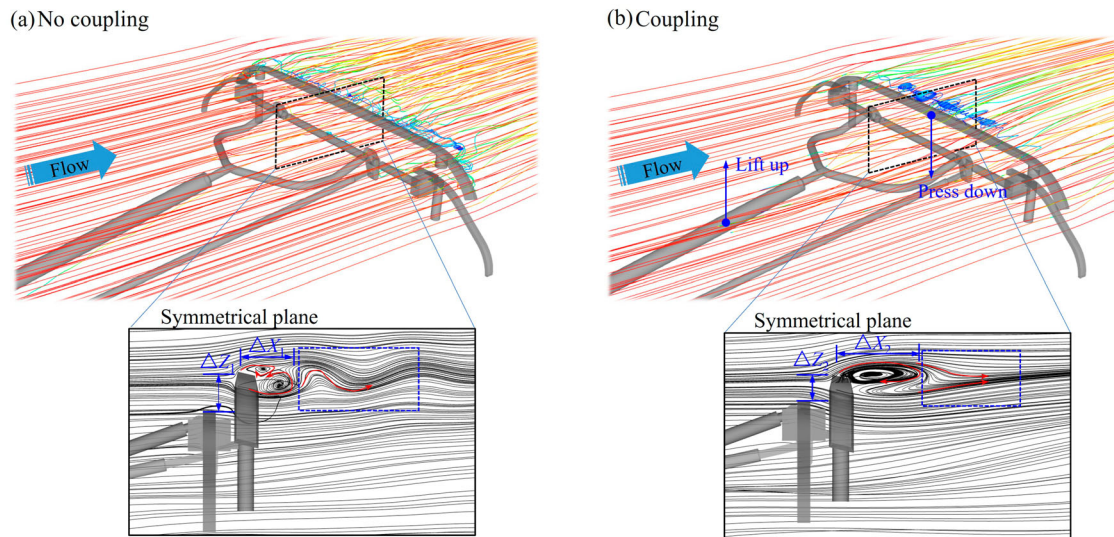


Figure 13. Streamlines at the pan-head calculated based on (a) CFD and (b) bidirectional coupling method under the speed of 450 km/h and pantograph in knuckle-upstream direction.

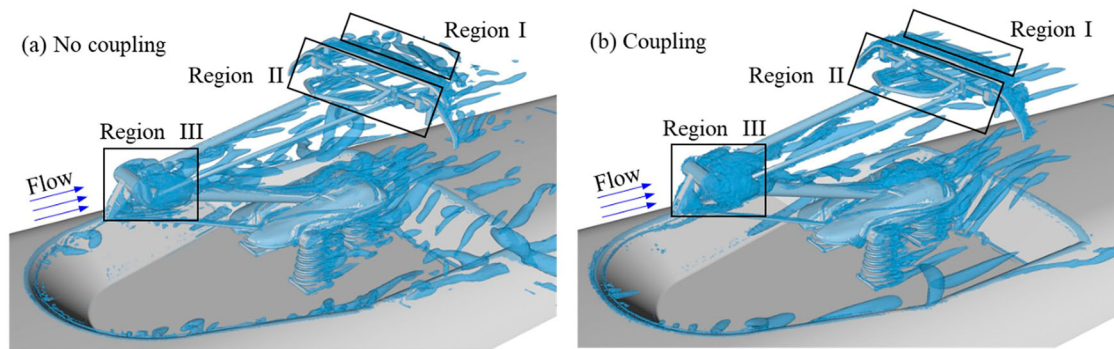


Figure 14. Iso-surface of Q-criterion ($2 \times 10^5 \text{ s}^{-1}$) for (a) uncoupling and (b) coupling conditions.

of the catenary. However, as shown by the blue boxes in Figure 15(a,c), both appear to fluctuate similarly to the shape of the catenary within one span. As shown by the blue boxes in Figure 15(b,d), unlike the lower arm rod, the fundamental frequency of the vibration response at the contact point was located in the high-frequency interval of 5–20 Hz, with a fundamental frequency of 14.992 Hz, and it connected its multiple frequencies by a folded line. From the figure, it can be observed that the folded-line crest frequency was more consistent with the orange line because the contact point vibration was intensified under aerodynamic excitation but constrained by the natural frequency of the system. The fundamental frequency of the contact point vibration was transferred from the low-frequency vibration of the pantograph passing through the registration arm to the high-frequency vibration passing through the dropper.

As shown in Figure 16, the acceleration distribution of each component of the pantograph during the contacting process of the PCS is contact strip > pan-head > upper

frame > lower arm rod, in which the contact strip vibrates the most fiercely. The maximal accelerations during the rising and falling process are 69.82 and -90.14 m/s^2 , respectively, and the acceleration of the upper frame and lower arm rod changes more gently. This was because the contact strip was at the end of the pantograph mechanism and directly interacts with the contact wire. The complex dynamic behaviours of the pantograph and contact network converge, which made it vibrate violently, and the falling acceleration of the contact strip was always larger than its rising acceleration under the downward pressure of the aerodynamic force. The red box in the figure showed that the falling process of the contact strip drives the motion of the pan-head; however, owing to the characteristics of the spring oscillator system, the motion of the pan-head has a certain hysteresis. It can be observed that the order of acceleration transfer in the pantograph mechanism was contact strip, pan-head, upper frame, and lower arm rod; therefore, the high-frequency vibration of the

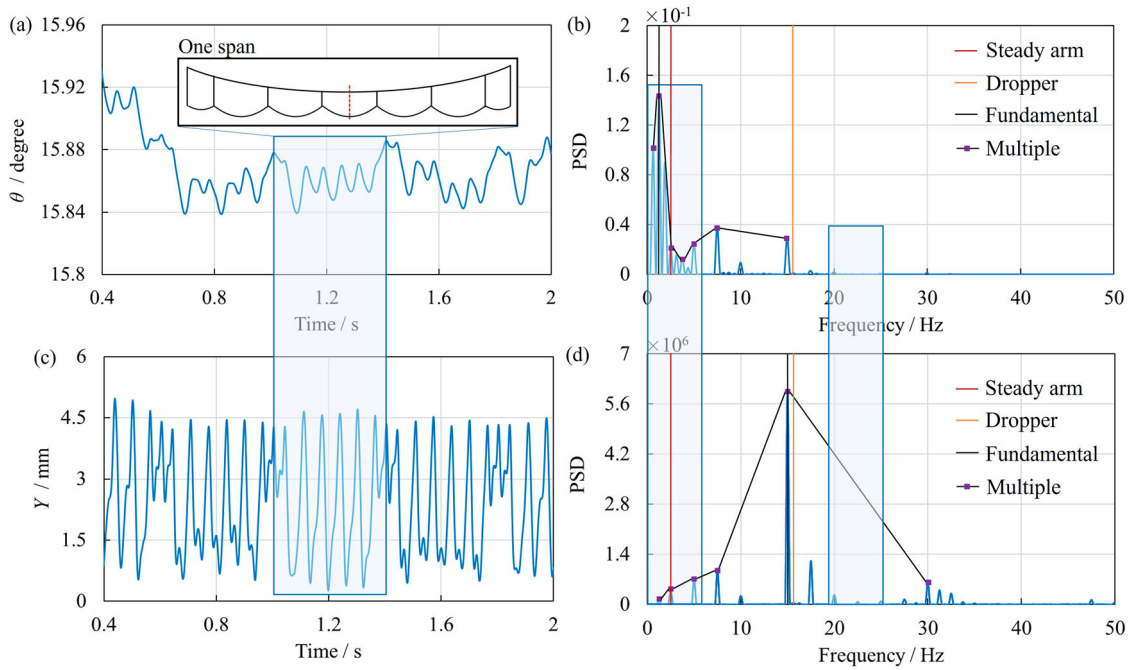


Figure 15. Time-domain and frequency-domain plots of the pantograph in the knuckle-upstream direction, (a,b) lower arm rod tilt angle and (c,d) contact point displacement under the speed of 450 km/h.

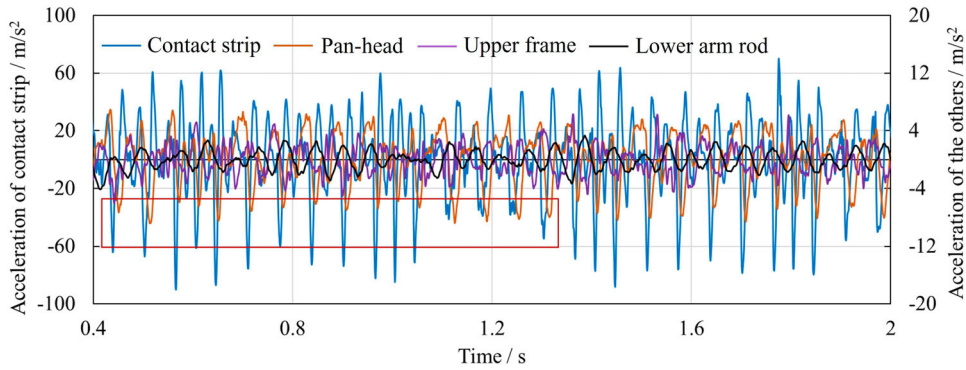


Figure 16. Time-history curves of acceleration of each component of the pantograph at 450 km/h, knuckle-upstream condition.

pantograph operation is mainly concentrated in the contact strip, and the pantograph frame composed of the lower arm rod, upper frame, and pull rod was dominated by the low-frequency vibration with a small amplitude, which was in line with the frequency domain analysis in Figure 12.

5.3. Interaction between pantograph and catenary

As shown in Figure 17(a), during train operation, the mean and standard deviation of the contact force of the PCS are 49.7 and 36.3 N. Under the action of aerodynamic excitation, the contact strip had a large vertical acceleration in downward direction at the highest point of the motion path, which led to a number of offline places of the PCS as shown by the red box in the figure. The longest offline time was 7 ms, with an offline rate

of 3.3%. As shown in Figure 17(b), similar to the contact point, the fundamental frequency of the contact force vibration is 14.981 Hz, and the two multiple-frequency folding line trends were similar. However, the main frequency of the contact force vibration was concentrated at 15–50 Hz, which was much larger than that of the contact point vibration.

6. Conclusions

In this study, a new method for the bidirectional coupling of aerodynamics and pantograph multi-body dynamics was proposed and validated to assess the coupling effect between the flow field around the pantograph and the dynamic behaviour of the pantograph. The main conclusions were as follows:

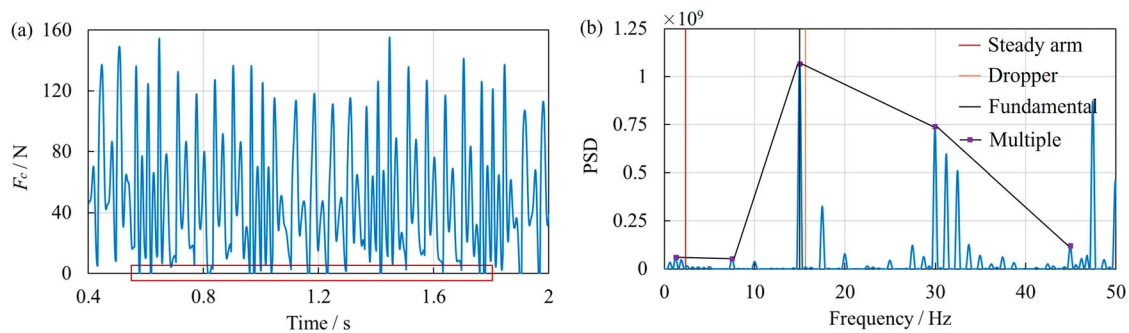


Figure 17. (a) Time-domain and (b) frequency-domain plots of the contact force between the pantograph in knuckle-upstream direction and the catenary under the speed of 450 km/h.

1. The accuracy of the model used for the pantograph flow field and dynamic simulations was verified at multiple levels. The constructed coupled flow – structure model can correctly characterise the coupling effect between the flow structures of the pantograph. Compared with the EN standard, it can obtain the real aerodynamic characteristics of the pantograph to realise real-time correction of the contact force of the PCS, which is more in line with the actual situation.
2. At the level of the aerodynamic characteristics of the pantograph, the amplitude and standard deviation of the aerodynamic lift force calculated by the bidirectional coupling method were smaller than those obtained using the CFD method. The motion of the pantograph components led to a larger difference between the separated vortex structure downstream of the contact strip calculated by the bidirectional coupling/CFD method and the backwash. This may be one of the reasons for the difference in standard deviation of the lift force of the contact strip between the two methods.
3. At the level of dynamic response of the PCS, when the pantograph in the knuckle-upstream direction was running at 450 km/h, under the action of aerodynamic downforce, the vibration of the contact strip was more violent, and the average value of the contact force of the PCS was at a lower level and fluctuates significantly, which was not conducive to the stable contact of the PCS. In addition, in the process of contact of the PCS, a number of offlines occurred, with the longest time offline being 7 ms, and the overall rate of offline being 3.3%.

The flow-induced vibration bidirectional coupling method proposed in this study updates the pantograph attitude based on overset grids, which can adapt to complex flow variations and provide high mesh resolution. However, the use of overset grids limits the selection of

turbulence models. In the future, a more accurate turbulence model can be selected based on the dynamic mesh technique to study the flow-induced vibration coupling effect of pantographs.

Author declarations

Disclosure statement

No potential conflict of interest was reported by the author(s).

Funding

This study was supported by the National Natural Science Foundation of China (52172359 and 52372363), National Key Research and Development Program of China (2023YFB4302502), Sichuan Province Central Guidance for Local Science and Technology Development Special Project (2023ZYD0019) and the Hebei Provincial Natural Science Foundation (E2022105032).

Author contributions

Zhuojun Li: Conceptualisation, Data curation, Formal analysis, Investigation, Methodology, Project administration, Validation, Writing original draft. **Chunjian Chen:** Methodology, Data Curation. **Huapu Song:** Data Curation. **Gang Yang:** Investigation, Supervision. **Jun Yang:** Conceptualisation, Investigation, Supervision. **Huadong Yao:** Conceptualisation, Investigation, Supervision. **Jiqiang Niu:** Writing, Review & Editing, Supervision, Project administration, Funding acquisition.

Data availability

The data that support the findings of this study are available from the corresponding authors upon reasonable request.

ORCID

Huadong Yao  <http://orcid.org/0000-0002-9547-7877>

References

- Amano, Y., Kobayashi, S., Yabuno, H., Yamashita, Y., & Mori, H. (2024). Mechanism and suppression of friction-induced vibration in catenary-pantograph system. *Nonlinear Dynamics*, 112(17), 14959–14980. <https://doi.org/10.1007/s11071-024-09802-6>
- Ambrósio, J., Pombo, J., Pereira, M., Antunes, P., & Mósca, A. (2012). A computational procedure for the dynamic analysis of the catenary-pantograph interaction in high-speed trains. *Journal of Theoretical and Applied Mechanics*, 50(3), 681–699.
- Bocciolone, M., Resta, F., Rocchi, D., Tosi, A., & Collina, A. (2006). Pantograph aerodynamic effects on the pantograph-catenary interaction. *Vehicle System Dynamics*, 44(sup1), 560–570. <https://doi.org/10.1080/00423110600875484>
- Brambilla, E., Carnevale, M., Facchinetti, A., & Rocchi, D. (2022). Influence of train roof boundary layer on the pantograph aerodynamic uplift: A proposal for a simplified evaluation method. *Journal of Wind Engineering and Industrial Aerodynamics*, 231, 105212. <https://doi.org/10.1016/j.jweia.2022.105212>
- Carnevale, M., Facchinetti, A., Maggiori, L., & Rocchi, D. (2015). Computational fluid dynamics as a means of assessing the influence of aerodynamic forces on the mean contact force acting on a pantograph. *Proceedings of the Institution of Mechanical Engineers, Part F*, 230(7), 1698–1713. <https://doi.org/10.1177/0954409715606748>
- Chang, C. (2010). *Hydrokinetic energy harnessing by enhancement of flow induced motion using passive turbulence control*. University of Michigan.
- Dai, Z., Li, T., Deng, J., Zhou, N., & Zhang, W. (2022a). Effect of the strip spacing on the aerodynamic performance of a high-speed double-strip pantograph. *Vehicle System Dynamics*, 60(10), 3358–3374. <https://doi.org/10.1080/00423114.2021.1945117>
- Dai, Z., Li, T., Zhou, N., Zhang, J., & Zhang, W. (2022b). Numerical simulation and optimization of aerodynamic uplift force of a high-speed pantograph. *Railway Engineering Science*, 30(1), 117–128. <https://doi.org/10.1007/s40534-021-00258-7>
- EN 14067–6. (2018). Railway applications-aerodynamics, part 6: Requirements and test procedures for cross wind assessment.
- EN 50119. (2020). Railway applications-fixed installations-electric traction overhead contact lines.
- EN 50317. (2012). Railway applications-current collection systems-requirements for and validation of measurements of the dynamic interaction between pantograph and overhead contact line.
- EN 50367. (2020). Railway applications-current collection systems-technical criteria for the interaction between pantograph and overhead line to achieve free access.
- Gai, J., Yu, Y., Wang, Y., Ding, Y., & Zhang, J. (2024). Improved delayed detached-eddy simulation on aerodynamic characteristics of biomimetic Coleoptera pantograph deflectors installed on a high-speed train. *Physics of Fluids*, 36(8), 085185. <https://doi.org/10.1063/5.0217245>
- Gregori, S., Tur, M., Nadal, E., Aguado, J. V., Fuenmayor, F. J., & Chinesta, F. (2017). Fast simulation of the pantograph-catenary dynamic interaction. *Finite Elements in Analysis and Design*, 129, 1–13. <https://doi.org/10.1016/j.finel.2017.01.007>
- Guo, J., Yang, S., & Gao, G. (2005). Research on active control of variable stiffness pantograph-catenary system. *Journal of Vibration and Shock*, 24(2), 9–11+15.
- Huan, R. H., Zhu, W. Q., Ma, F., & Ying, Z. G. (2014). Vertical dynamics of a pantograph carbon-strip suspension under stochastic contact-force excitation. *Nonlinear Dynamics*, 76(1), 765–776. <https://doi.org/10.1007/s11071-013-1167-2>
- Ji, Z., Guo, Y., Guo, D., Yang, G., & Liu, Y. (2021). Effects of running speed on coupling between pantograph of high-speed train and tunnel based on aerodynamics and multi-body dynamics coupling. *Applied Sciences*, 11(21), 10008.
- Kim, S. J., Kwon, H., & Ahn, J. (2023). Aerodynamic performance of a pantograph cover for high-speed train. *Journal of Mechanical Science and Technology*, 37(9), 4681–4693. <https://doi.org/10.1007/s12206-023-0823-9>
- Kulkarni, S., Pappalardo, C. M., & Shabana, A. A. (2016). Pantograph/catenary contact formulations. *Journal of Vibration and Acoustics*, 139(1), 011010. <https://doi.org/10.1115/1.4035132>
- Layukallo, T., & Nakamura, Y. (2003). Passive separation control on a square cylinder at transonic speed. *Transactions of the Japan Society for Aeronautical and Space Sciences*, 45(150), 236–242. <https://doi.org/10.2322/tjsass.45.236>
- Li, R., Zhang, W., Ning, Z., Liu, B., Zou, D., & Liu, W. (2016). Influence of a high-speed train passing through a tunnel on pantograph aerodynamics and pantograph-catenary interaction. *Proceedings of the Institution of Mechanical Engineers, Part F*, 231(2), 198–210. <https://doi.org/10.1177/0954409715626743>
- Li, X., Zhou, D., Jia, L., & Yang, M. (2018). Effects of yaw angle on the unsteady aerodynamic performance of the pantograph of a high-speed train under crosswind. *Journal of Wind Engineering and Industrial Aerodynamics*, 182, 49–60. <https://doi.org/10.1016/j.jweia.2018.09.009>
- Liu, H., Chen, R., Zhou, S., Gao, Y., Zou, Y., Liu, T., & Zhao, Y. (2023). Numerical study on the effect of pantograph fairing on aerodynamic performance at various train heights. *Engineering Applications of Computational Fluid Mechanics*, 17(1), 2261521. <https://doi.org/10.1080/19942060.2023.2261521>
- Liu, Z., Song, Y., Gao, S., & Wang, H. (2024). Review of perspectives on pantograph-catenary interaction research for high-speed railways operating at 400 km/h and above. *IEEE Transactions on Transportation Electrification*, 10(3), 7236–7257. <https://doi.org/10.1109/TTE.2023.3346379>
- Liu, H., Zhang, S., Liang, X., & Zou, Y. (2022). The effect of covering structure in pantograph sinking platform on the aerodynamics of high-speed train. *Engineering Applications of Computational Fluid Mechanics*, 16(1), 2157–2175. <https://doi.org/10.1080/19942060.2022.2133517>
- Massat, J. P., Laine, J. P., & Bobillot, A. (2006). Pantograph-catenary dynamics simulation. *Vehicle System Dynamics*, 44(sup1), 551–559. <https://doi.org/10.1080/00423110600875443>
- Mei, G., Luo, Q., Qiao, W., Huang, Z., Lu, J., & Wang, J. (2022). Study of load spectrum compilation method for the pantograph upper frame based on multi-body dynamics. *Engineering Failure Analysis*, 135, 106099. <https://doi.org/10.1016/j.engfailanal.2022.106099>

- Ouyang, M., Chen, S., Li, Q., & Yang, Z. (2022). Numerical investigation on aerodynamic forces and flow patterns of high-speed trains from open air into long tunnel. *Journal of Wind Engineering and Industrial Aerodynamics*, 229, 105142. <https://doi.org/10.1016/j.jweia.2022.105142>
- Pappalardo, C. M., Patel, M. D., Tinsley, B., & Shabana, A. A. (2015). Contact force control in multibody pantograph/catenary systems. *Proceedings of the Institution of Mechanical Engineers, Part K*, 230(4), 307–328. <https://doi.org/10.1177/1464419315604756>
- Pombo, J., & Ambrósio, J. (2012). Influence of pantograph suspension characteristics on the contact quality with the catenary for high speed trains. *Computers & Structures*, 110–111, 32–42. <https://doi.org/10.1016/j.compstruc.2012.06.005>
- Pombo, J., & Ambrósio, J. (2013). Environmental and track perturbations on multiple pantograph interaction with catenaries in high-speed trains. *Computers & Structures*, 124, 88–101. <https://doi.org/10.1016/j.compstruc.2013.01.015>
- Qin, D., Li, T., Zhou, N., & Zhang, J. (2024). Aerodynamic drag and noise reduction of a pantograph of high-speed trains with a novel cavity structure. *Physics of Fluids*, 36(2), 027108. <https://doi.org/10.1063/5.0188831>
- Rong, B., Rui, X., Tao, L., & Wang, G. (2019). Theoretical modeling and numerical solution methods for flexible multibody system dynamics. *Nonlinear Dynamics*, 98(2), 1519–1553. <https://doi.org/10.1007/s11071-019-05191-3>
- Seo, J. H., Sugiyama, H., & Shabana, A. A. (2005). Three-dimensional large deformation analysis of the multibody pantograph/catenary systems. *Nonlinear Dynamics*, 42(2), 199–215. <https://doi.org/10.1007/s11071-005-2789-9>
- Song, Y., Mei, G., Liu, Z., & Gao, S. (2024). Assessment of railway pantograph-catenary interaction performance with realistic pantograph strip imperfection. *Vehicle System Dynamics*, 62(9), 2355–2374. <https://doi.org/10.1080/00423114.2023.2289662>
- Song, Y., Ouyang, H., Liu, Z., Mei, G., Wang, H., & Lu, X. (2017). Active control of contact force for high-speed railway pantograph-catenary based on multi-body pantograph model. *Mechanism and Machine Theory*, 115, 35–59. <https://doi.org/10.1016/j.mechmachtheory.2017.04.014>
- Song, Y., Rønquist, A., & Nāvīk, P. (2020). Assessment of the high-frequency response in railway pantograph-catenary interaction based on numerical simulation. *IEEE Transactions on Vehicular Technology*, 69(10), 10596–10605. <https://doi.org/10.1109/TVT.2020.3015044>
- Tur, M., Baeza, L., Fuenmayor, F. J., & García, E. (2015). Pacdin statement of methods. *Vehicle System Dynamics*, 53(3), 402–411. <https://doi.org/10.1080/00423114.2014.963126>
- Wang, W., Liang, Y., Zhang, W., & Iwnicki, S. (2019). Effect of the nonlinear displacement-dependent characteristics of a hydraulic damper on high-speed rail pantograph dynamics. *Nonlinear Dynamics*, 95(4), 3439–3464. <https://doi.org/10.1007/s11071-019-04766-4>
- Wang, D., Sun, C., Liu, X., Wang, Z., & Li, R. (2024). Flow-induced vibration analysis by simulating a high-speed train pantograph. *Applied Sciences*, 14(11), 4493.
- Wu, Z., Xie, Z., Wang, P., & Ding, W. (2020). Aerodynamic drag performance analysis of different types of high-speed train pantograph fairing. *Journal of Applied Science and Engineering*, 23(3), 509–519. [https://doi.org/10.6180/jase.202009_23\(3\).0015](https://doi.org/10.6180/jase.202009_23(3).0015)
- Xiao, C., Yang, M., Tan, C., & Lu, Z. (2020). Effects of platform sinking height on the unsteady aerodynamic performance of high-speed train pantograph. *Journal of Wind Engineering and Industrial Aerodynamics*, 204, 104284. <https://doi.org/10.1016/j.jweia.2020.104284>
- Zhao, Y.-Y., Yang, Z.-G., Li, Q.-L., & Xia, C. (2020). Analysis of the near-field and far-field sound pressure generated by high-speed trains pantograph system. *Applied Acoustics*, 169, 107506. <https://doi.org/10.1016/j.apacoust.2020.107506>
- Zhou, N., & Zhang, W. (2011). Investigation on dynamic performance and parameter optimization design of pantograph and catenary system. *Finite Elements in Analysis and Design*, 47(3), 288–295. <https://doi.org/10.1016/j.finel.2010.10.008>